Calibrationless OSCAR-based Image Reconstruction in Compressed Sensing Parallel MRI

L. El Gueddari [1,2], P. Ciuciu[1,2], E. Chouzenoux [3,4], A. Vignaud [1] and J-C. Pesquet[3]

[1]CEA/NeuroSpin, Gif-sur-Yvette, France

[2]INRIA-CEA Saclay Ile-de-France, Parietal team, Univ Paris-Saclay, France

[3]CVN, Centrale-Supélec, Univ. Paris-Saclay, France

[4]LIGM, Paris-Est University, France

ISBI, 2019, Venice, Italy

Outline

Outline

Anatomical MRI

Anatomical MRI is generally acquired using Cartesian sampling.

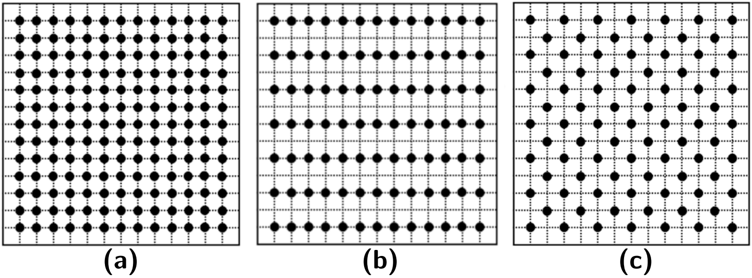

Figure: Typical **(a)** Cartesian **(b)** parallel acquisition **(c)** CAIPIRINHA[1] acquisition

... however in some cases non-Cartesian trajectories are useful ...

[1] Breuer et al. 2006, *Magnetic Resonance in Medicine*.

Non-Cartesian trajectories for anatomical MRI

A non-exhaustive list of usage

- For ultra-short echo time imaging[2]
- X-nuclei imaging (TPI[3])
- To correct for motion, especially for abdominopelvic MRI[4]

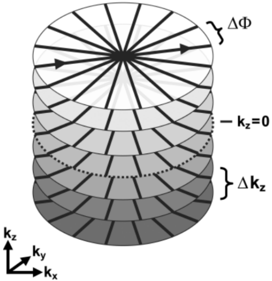

Figure: Stack of stars used for VIBE acquisition

[2] Johnson et al. 2013, *Magnetic Resonance in Medicine*.
[3] Boada et al. 1997, *Magnetic Resonance in Medicine*.
[4] Chandarana et al. 2014, *European radiology*.

Non-Cartesian trajectories for anatomical MRI

A non-exhaustive list of usage

- For ultra-short echo time imaging[2]
- X-nuclei imaging (TPI[3])
- To correct for motion, especially for abdominopelvic MRI[4]

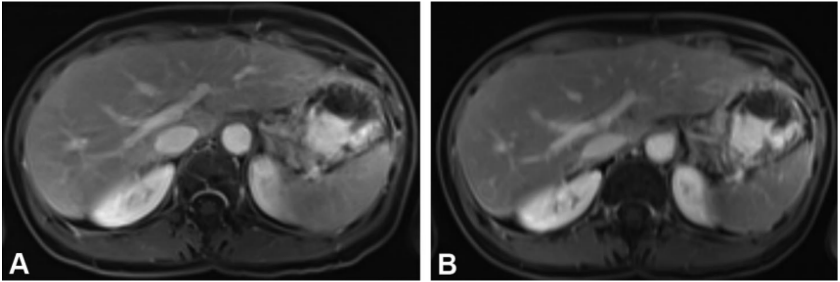

Figure: A: Free-breathing stack-of-stars VIBE, B: Breath-holding conventional VIBE

[2] Johnson et al. 2013, *Magnetic Resonance in Medicine*.
[3] Boada et al. 1997, *Magnetic Resonance in Medicine*.
[4] Chandarana et al. 2014, *European radiology*.

Non-Cartesian trajectories for anatomical MRI

Renewed interest to speed-up acquisition in the context of Compressed Sensing[5].

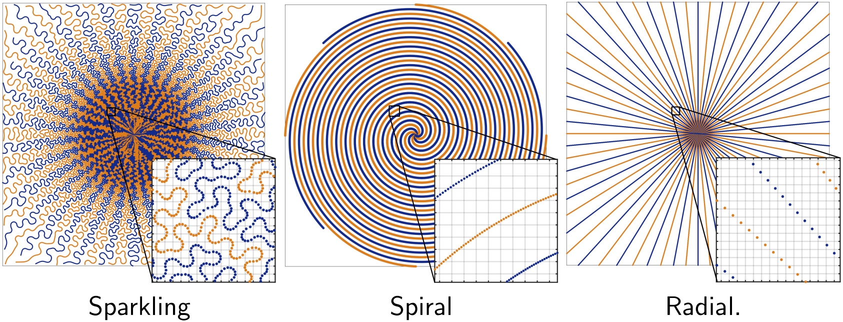

Figure: Example of non-Cartesian trajectories.

[5] Lazarus et al. 2019, *Magnetic Resonance in Medicine*.

Non-Cartesian trajectories for anatomical MRI

Renewed interest to speed-up acquisition in the context of Compressed Sensing[5].

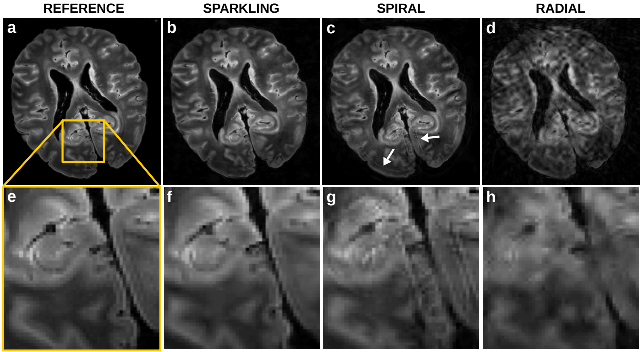

Figure: Comparison of different acquisition trajectories with 16-fold accelerated acquisition on T2*-weighted images.

[5] Lazarus et al. 2019, *Magnetic Resonance in Medicine*.

Non-Cartesian trajectories for anatomical MRI

Parallel imaging acquisition: collect multiple k-space data using a multi-receiver coil as the latter is known to boost the SNR.

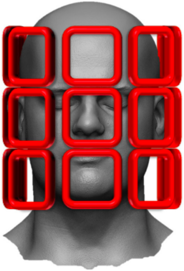

Illustration of multi-receiver coil (phased array).

Roemer et al. 1990, *Magnetic Resonance in Medicine*.

How do we reconstruct MR images from non-Cartesian k-space measurements in parallel imaging?

Non-Cartesian MR image reconstruction in parallel imaging

Self-calibrating methods

Non-Cartesian reconstruction techniques can be split in two categories:

1. Self-calibrating methods:

[7] Samsonov et al. 2004, *Magnetic Resonance in Medicine*.
[8] Uecker et al. 2014, *Magnetic Resonance in Medicine*.

Non-Cartesian reconstruction techniques can be split in two categories:

1. Self-calibrating methods:
    - require a region where the signal has been sampled at least at the Nyquist rate

[7] Samsonov et al. 2004, *Magnetic Resonance in Medicine*.
[8] Uecker et al. 2014, *Magnetic Resonance in Medicine*.

Non-Cartesian reconstruction techniques can be split in two categories:

1. Self-calibrating methods:
   - require a region where the signal has been sampled at least at the Nyquist rate
   - model the coil sensitivity profiles $\boldsymbol{S}_\ell$ for all channels $\ell = 1, \dots, L$ [7,8]

[7] Samsonov et al. 2004, *Magnetic Resonance in Medicine*.
[8] Uecker et al. 2014, *Magnetic Resonance in Medicine*.

Non-Cartesian reconstruction techniques can be split in two categories:

1. Self-calibrating methods:
    - require a region where the signal has been sampled at least at the Nyquist rate
    - model the coil sensitivity profiles $\boldsymbol{S}_\ell$ for all channels $\ell = 1, \ldots, L$[7,8]
    - solve an inverse problem and recover a single full FOV image:

$$\widehat{\boldsymbol{x}} = \operatorname*{arg\,min}_{\boldsymbol{x} \in \mathbb{C}^N} \frac{1}{2} \sum_{\ell=1}^{L} \sigma_\ell^{-2} \| \boldsymbol{F}_\Omega \boldsymbol{S}_\ell \boldsymbol{x} - \boldsymbol{y}_\ell \|_2^2 + \lambda \| \boldsymbol{\Psi} \boldsymbol{x} \|_1 \quad (1)$$

[7] Samsonov et al. 2004, *Magnetic Resonance in Medicine*.
[8] Uecker et al. 2014, *Magnetic Resonance in Medicine*.

Non-Cartesian reconstruction techniques can be split in two categories:

1. Self-calibrating methods:
   - require a region where the signal has been sampled at least at the Nyquist rate
   - model the coil sensitivity profiles $\boldsymbol{S}_\ell$ for all channels $\ell = 1, \ldots, L$ [7,8]
   - solve an inverse problem and recover a single full FOV image:

$$\widehat{\boldsymbol{x}} = \underset{\boldsymbol{x} \in \mathbb{C}^N}{\arg\min} \frac{1}{2} \sum_{\ell=1}^{L} \sigma_\ell^{-2} \| \boldsymbol{F}_\Omega \boldsymbol{S}_\ell \boldsymbol{x} - \boldsymbol{y}_\ell \|_2^2 + \lambda \| \boldsymbol{\Psi} \boldsymbol{x} \|_1 \quad (1)$$

Note: Extraction of coil sensitivity maps is challenging in non-Cartesian case

[7] Samsonov et al. 2004, *Magnetic Resonance in Medicine*.
[8] Uecker et al. 2014, *Magnetic Resonance in Medicine*.

Non-Cartesian reconstruction techniques can be split in two categories:

2. Calibration-less methods:
   - do not require any calibration region

[9] Trzasko and Manduca 2011, *Signals, Systems and Computers (ASILOMAR), 2011 Conference Record of the Forty Fifth Asilomar Conference on*.

[10] Majumdar and Ward 2012, *Magnetic Resonance in Medicine*.

Non-Cartesian MR Image reconstruction from multi-channel array coil acquisition

Calibration-less methods

Non-Cartesian reconstruction techniques can be split in two categories:

2. Calibration-less methods:
   - do not require any calibration region
   - solve an inverse problem but recover channel-specific images

[9] Trzasko and Manduca 2011, *Signals, Systems and Computers (ASILOMAR), 2011 Conference Record of the Forty Fifth Asilomar Conference on*.

[10] Majumdar and Ward 2012, *Magnetic Resonance in Medicine*.

Non-Cartesian MR Image reconstruction from multi-channel array coil acquisition

Calibration-less methods

Non-Cartesian reconstruction techniques can be split in two categories:

2. Calibration-less methods:
    - do not require any calibration region
    - solve an inverse problem but recover channel-specific images
    - use the redundant information given by each coil to impose constraints such as low-rank CLEAR[9] or group-sparsity CALM[10]

[9] Trzasko and Manduca 2011, *Signals, Systems and Computers (ASILOMAR), 2011 Conference Record of the Forty Fifth Asilomar Conference on*.

[10] Majumdar and Ward 2012, *Magnetic Resonance in Medicine*.

Non-Cartesian reconstruction techniques can be split in two categories:

2. Calibration-less methods:
   - do not require any calibration region
   - solve an inverse problem but recover channel-specific images
   - use the redundant information given by each coil to impose constraints such as low-rank CLEAR[9] or group-sparsity CALM[10]
   - more likely to be used for on-line image reconstruction

[9] Trzasko and Manduca 2011, *Signals, Systems and Computers (ASILOMAR), 2011 Conference Record of the Forty Fifth Asilomar Conference on*.
[10] Majumdar and Ward 2012, *Magnetic Resonance in Medicine*.

Outline

1. Motivation & Context
   - Why non-Cartesian acquisition
   - Non-Cartesian MR mage reconstruction in parallel imaging
2. Calibration-less MR image reconstruction
   - Problem statement
   - Joint sparsity regularization
3. Experiments & Results
   - Experimental set-up
   - Results
4. Conclusion & Discussion

Problem statement

Calibration-less MR image reconstruction problem solved using an *analysis formulation*:

Definition

MR image reconstruction is formulated as follows:

$$\underline{\widehat{\boldsymbol{x}}} = \operatorname*{arg\,min}_{\underline{\boldsymbol{x}} \in \mathbb{C}^{N \times L}} \Big\{ \frac{1}{2} \sum_{\ell=1}^{L} \sigma_\ell^{-2} \| F_\Omega \boldsymbol{x}_\ell - \boldsymbol{y}_\ell \|_2^2 + g(\boldsymbol{T} \underline{\boldsymbol{x}}) \Big\}, \quad (2)$$

with:

- $\boldsymbol{y}_\ell \in \mathbb{C}^M$ the $\ell^{\textbf{th}}$ channel-specific data set
- $\boldsymbol{x}_\ell \in \mathbb{C}^N$ the $\ell^{\textbf{th}}$ channel-specific reconstructed image (ex. $N = 512 \times 512$)
- F_Ω is the forward under-sampling Fourier operator
- $\boldsymbol{T} \in \mathbb{C}^{N_\Psi \times N}$ linear operator related to a sparse decomposition
- g is a convex regularization term that promotes sparsity

We aim to find:

$$\widehat{\underline{\boldsymbol{x}}} \in \underset{\underline{\boldsymbol{x}} \in \mathbb{C}^{N \times L}}{\operatorname{argmin}} \left[f(\underline{\boldsymbol{x}}) + g(\boldsymbol{T}\underline{\boldsymbol{x}}) \right] \tag{3}$$

where:

- f is convex, differentiable on $\mathbb{C}^{N \times L}$ and its gradient is β-Lipschitz
- $g \in \Gamma_0(\mathbb{C}^{N_\Psi \times L})$ with a closed form proximity operator, given by:

$$\operatorname{prox}_g(\underline{\boldsymbol{z}}) = \underset{\boldsymbol{v} \in \mathbb{C}^{N_\Psi \times L}}{\operatorname{argmin}} \frac{1}{2} \|\underline{\boldsymbol{z}} - \boldsymbol{v}\|^2 + g(\boldsymbol{v}) \tag{4}$$

Note: Those are standard assumption in optimization based image reconstruction methods.

Using a primal-dual optimization method proposed by Condat-Vũ[11,12]:

Algorithm 1: Condat-Vũ algorithm

initialize $k = 0$, $\tau > 0$, $\kappa > 0$, $\underline{\boldsymbol{x}}_0$, $\underline{\boldsymbol{z}}_0$;
while $k \leq K$ **do**

$$\underline{\boldsymbol{x}}_{k+1} := \underline{\boldsymbol{x}}_k - \tau \left(\nabla f(\underline{\boldsymbol{x}}_k) + \boldsymbol{T}^* \underline{\boldsymbol{z}}_k\right);$$
$$\underline{\boldsymbol{w}}_{k+1} := \underline{\boldsymbol{z}}_k + \kappa \boldsymbol{T} \left(2\underline{\boldsymbol{x}}_{k+1} - \underline{\boldsymbol{x}}_k\right);$$
$$\underline{\boldsymbol{z}}_{k+1} := \underline{\boldsymbol{w}}_{k+1} - \kappa \operatorname{prox}_{g/\kappa}\left(\frac{\underline{\boldsymbol{w}}_{k+1}}{\kappa}\right);$$

end

with:

- the algorithm weakly converges to the solution of Eq. (3) if

$$\frac{1}{\tau} - \kappa |||\boldsymbol{T}|||^2 \geq \frac{\beta}{2}$$

- τ and κ hyper-parameters set as follows: $\tau := \dfrac{1}{\beta}$, $\kappa := \dfrac{\beta}{2|||\boldsymbol{T}|||^2}$

[11] Condat 2013, *Journal of Optimization Theory and Applications*.

[12] Vũ 2013, *Advances in Computational Mathematics*.

Joint sparsity regularization

Group-LASSO

Parallel imaging has been proved to have tighter recovery guarantees than single channel acquisition when combined with Group-LASSO (GL) regularization[13].

Definition

The group-LASSO penalty is defined as follows:

$$g_{\mathrm{GL}}(\underline{z}) = \|\underline{z}\|_{1,2} \quad = \sum_{s=1}^{S} \left(\lambda \gamma^s \sum_{p=1}^{P_s} \sqrt{\sum_{\ell=1}^{L} |z_{sp\ell}|^2} \right)$$

- λ and γ are positive hyper-parameters
- s models the scale or subband dependence

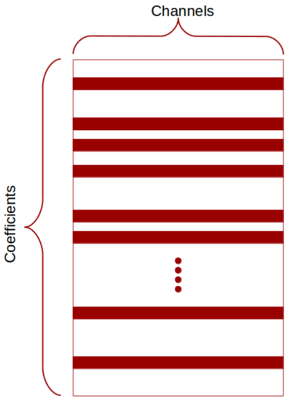

[13] Chun, Adcock, and Talavage 2016, *IEEE Transactions on Medical Imaging*.
For $\gamma = 1$ the algorithm corresponds to Majumdar and Ward, *Magnetic Resonance in Medicine*, 2012

Variant: Sparse group-LASSO[15] (sGL)

Definition

$$\forall \underline{z} \in \mathbb{C}^{N_\Psi \times L}, g_{\mathrm{sGL}}(\underline{z}) = g_{\mathrm{GL}}(\underline{z}) + \mu \|\underline{z}\|_1 \quad (5)$$

- μ being positive hyper-parameter.

sGL proximity operator[18] is closed form and corresponds to the composition of GL proximity operator with soft-thresholding.

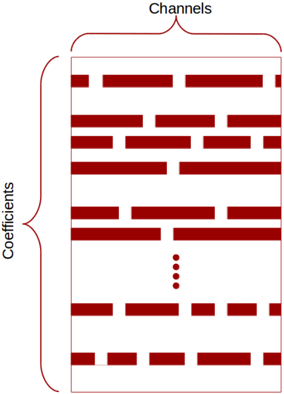

[15] Friedman, Hastie, and Tibshirani 2010, *arXiv preprint arXiv:1001.0736*.

Joint sparsity regularization

Octagonal Shrinkage and Clustering Algorithm for Regression

Inferring the structure via a pairwise ℓ_∞ norm.
OSCAR regularization[16]:

Definition

$$g_{\mathrm{OSCAR}}(\boldsymbol{z}) = \sum_{s=1}^{S} \lambda \left[\sum_{j=1}^{P_s L} |z_{sj}| + \gamma \sum_{j<k} \max\{|z_{sj}|, |z_{sk}|\} \right]$$
$$= \sum_{s=1}^{S} \lambda \left[\sum_{j=1}^{P_s L} (\gamma(j-1)+1) \, |z_{sj}|_{\downarrow} \right] \quad (6)$$

where:

- $\boldsymbol{z}_{\downarrow} \in \mathbb{C}^{N_\Psi \times L}$ the wavelet coefficients sorted in decreasing order, i.e.: $\forall s \in \mathbb{N}, |z_{s1}| \leq \cdots \leq |z_{sP_s L}|$.
- λ and γ are some positive hyper-parameters that need to be set

[16] Bondell and Reich 2008, *Biometrics*.

Outline

Experimental set-up

Sequence parameters:

- Ex-vivo baboon brain
- 7T Siemens Scanner GRE
- 1Tx/32Rx Nova coil
- Sparkling trajectory
- 390μm$\times$390μm in plane-resolution
- 3mm slice thickness
- Acceleration factor of 15 in time
- Under-sampling factor of 2.5
- $\boldsymbol{T}$: Undecimated Bi-Orthogonal 7-9 wavelet transform

Hyper-parameters set using a grid-search procedure.
Cartesian scan 512$\times$512 was acquired and used for reference.

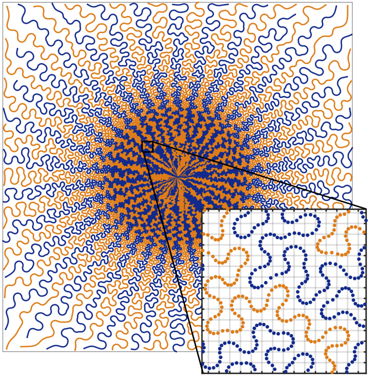

Figure: Sparkling trajectory

Coil combination: Square root of the Sum-Of-Squares
Structural SIMilarity Index (SSIM)[17] used to set hyper-parameters

Table: Image quality assessment for all regularizers.

	SSIM	pSNR (dB)	NRMSE
IFT	0.847	26.50	0.263
GL	0.864	26.92	0.254
sGL	0.851	26.77	0.259
OSCAR	**0.875**	**30.49**	**0.177**
ℓ_1-ESPIRiT	0.874	28.32	0.238

Note: ℓ_1-ESPIRiT is a self-calibrating method.

[17] Wang et al. 2004, *IEEE transactions on image processing*.

Results

Comparison of the Sum-Of-Squares

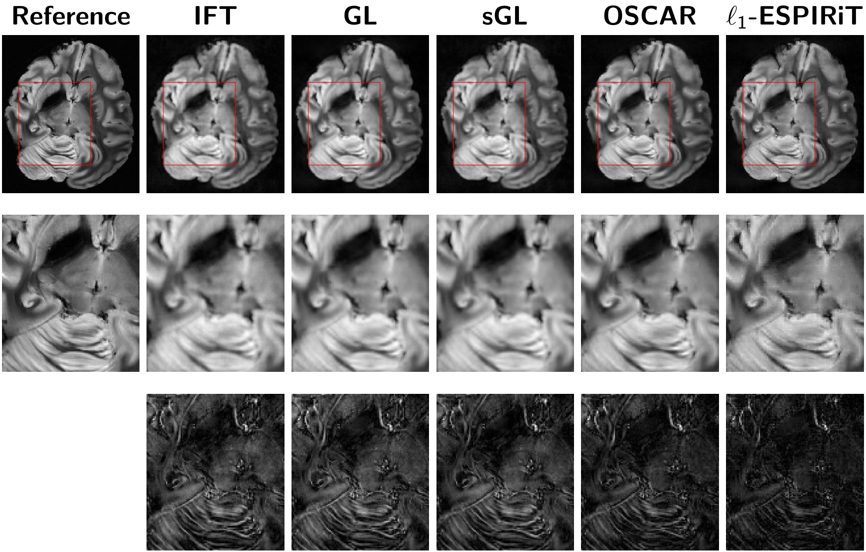

Results

Quantitative assessment

Comparison between coil images:

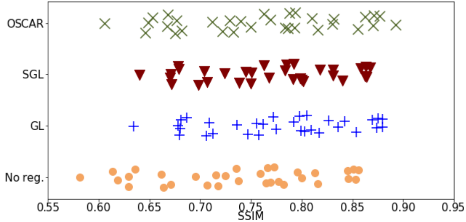

Figure: Assessment of the SSIM score per channel.

Comparison between coil images:

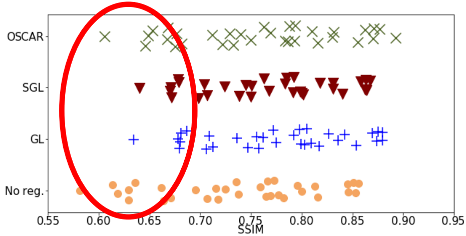

Figure: Assessment of the SSIM score per channel.

Results

Comparison of the image channels: low-SNR channel

No reg.	Group-LASSO	Sparse GL	OSCAR
SSIM= 0.630	SSIM= 0.680	SSIM= 0.672	SSIM= 0.646

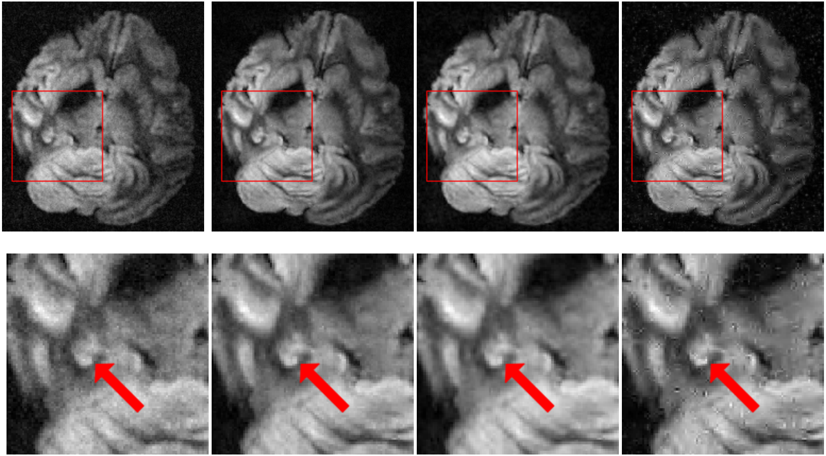

Results

Quantitative assessment

Comparison between coil images:

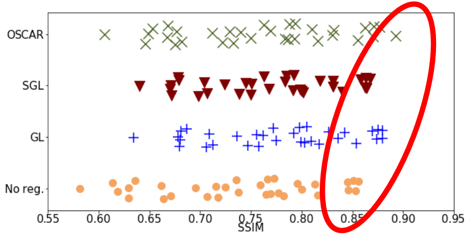

Figure: Assessment of the SSIM score per channel.

Results

Comparison of the image channels: high-SNR channel

No reg.	Group-LASSO	Sparse GL	OSCAR
SSIM= 0.846	SSIM= 0.880	SSIM= 0.863	SSIM= 0.893

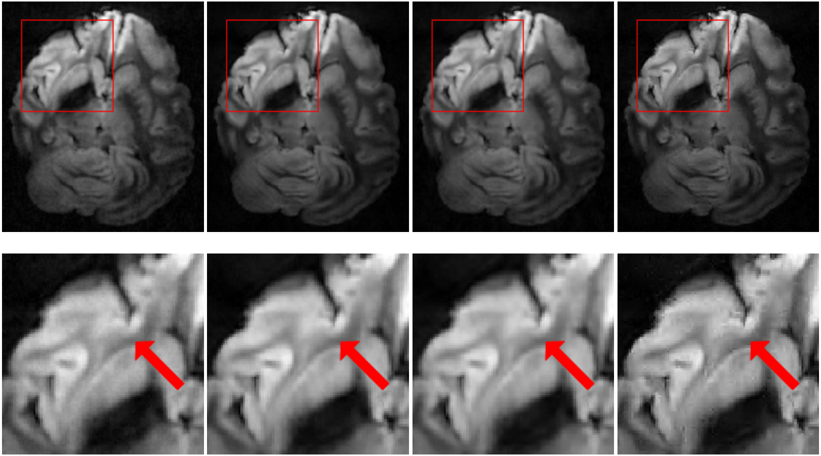

Outline

Conclusion & Discussion

Conclusion:

- New parallel CS-MRI reconstruction algorithm
- No sensitivity maps
- OSCAR outperforms group-LASSO and sparse group-LASSO
- OSCAR and ℓ_1-ESPIRiT are comparable, however the latest is self-calibrating
- Same optimization method to solve calibration-less MR reconstruction

Perspective:

- Extension to 3D-MRI
- Study motion impact on the reconstruction

Boada, Fernando E. et al. (1997). "Fast three dimensional sodium imaging". In: *Magnetic Resonance in Medicine* 37.5, pp. 706–715.

Bondell, H.D. and B.J. Reich (2008). "Simultaneous regression shrinkage, variable selection, and supervised clustering of predictors with OSCAR". In: *Biometrics* 64.1, pp. 115–123.

Breuer, Felix A et al. (2006). "Controlled aliasing in volumetric parallel imaging (2D CAIPIRINHA)". In: *Magnetic Resonance in Medicine* 55.3, pp. 549–556.

Chandarana, Hersh et al. (2014). "Free-breathing contrast-enhanced T1-weighted gradient-echo imaging with radial k-space sampling for paediatric abdominopelvic MRI". In: *European radiology* 24.2, pp. 320–326.

Chun, I.Y., B. Adcock, and T.M. Talavage (2016). "Efficient compressed sensing SENSE pMRI reconstruction with joint sparsity promotion". In: *IEEE Transactions on Medical Imaging* 35.1, pp. 354–368.

Condat, L. (2013). "A primal–dual splitting method for convex optimization involving Lipschitzian, proximable and linear composite terms". In: *Journal of Optimization Theory and Applications* 158.2, pp. 460–479.

Friedman, J., T. Hastie, and R. Tibshirani (2010). "A note on the group lasso and a sparse group lasso". In: *arXiv preprint arXiv:1001.0736*.

Johnson, Kevin M. et al. (2013). "Optimized 3D ultrashort echo time pulmonary MRI". In: *Magnetic Resonance in Medicine* 70.5, pp. 1241–1250.

Lazarus, Carole et al. (2019). "SPARKLING: variable-density k-space filling curves for accelerated T2*-weighted MRI". In: *Magnetic Resonance in Medicine* 81.6, pp. 3643–3661.

Majumdar, A.l and R.K. Ward (2012). "Calibration-less multi-coil MR image reconstruction". In: *Magnetic Resonance in Medicine* 30.7, pp. 1032–1045.

Roemer, P.B. et al. (1990). "The NMR phased array". In: *Magnetic Resonance in Medicine* 16.2, pp. 192–225.

Samsonov, Alexei A et al. (2004). "POCSENSE: POCS-based reconstruction for sensitivity encoded magnetic resonance imaging". In: *Magnetic Resonance in Medicine* 52.6, pp. 1397–1406.

Trzasko, J.D. and A. Manduca (2011). "Calibrationless parallel MRI using CLEAR". In: IEEE, pp. 75–79.

Uecker, M. et al. (2014). "ESPIRiT– an eigenvalue approach to autocalibrating parallel MRI: where SENSE meets GRAPPA". In: *Magnetic Resonance in Medicine* 71.3, pp. 990–1001.

Vũ, BC (2013). "A splitting algorithm for dual monotone inclusions involving cocoercive operators". In: *Advances in Computational Mathematics* 38.3, pp. 667–681.

Wang, Zhou et al. (2004). "Image quality assessment: from error visibility to structural similarity". In: *IEEE transactions on image processing* 13.4, pp. 600–612.